Manuscript

Bi off-centering in Centrosymmetric BiOBr Leading to Ultrahigh Bifunctional Piezocatalytic Fuel Generation Efficiencies in Seawater

Maqsuma Banoo,[a] Kushal Samanta,[b] Arjun Kumar Sah,[a] Raj Sekhar Roy,[a] Monika Bhakar,[c] Dirtha Sanyal,[d],[e] Digamber G. Porob,[f] Konstantin Glazyrin,[g] Dinesh Topwal,[h],[i] Goutam Sheet,[c] Dibyajyoti Ghosh,[b] Ujjal K. Gautam[a]*

[a]Department of Chemical Sciences, Indian Institute of Science Education and Research (IISER)-Mohali, Sector 81, Mohali, S.A.S. Nagar, Punjab 140306, India
[b]Department of Materials Science and Engineering, Indian Institute of Technology Delhi, Hauz Khas, New Delhi 110016, India

[c]Department of Physical Sciences, Indian Institute of Science Education and Research (IISER)-Mohali, Sector 81, Mohali, SAS Nagar, Punjab 140306, India.

[d]Homi Bhabha National Institute, Anushakti Nagar, Mumbai 400094, India

[e]Variable Energy Cyclotron Centre, 1/AF Bidhannagar, Kolkata 700064, India

[f]School of Chemical Sciences, Goa University, Taleigao Plateau, Goa- 403206, India

[g]Deutsches Elektronen-Synchrotron DESY, Notkestr. 85, 22607 Hamburg, Germany

[h]Institute of Physics Sachivalaya Marg, Bhubaneswar 751005, India

[i]Training School Complex, Homi Bhabha National Institute, Mumbai 400094, India

**Corresponding author: ujjalgautam@iisermohali.ac.in, ujjalgautam@gmail.com*

Abstract: Piezocatalytic water-splitting to simultaneously produce H_2 and H_2O_2 has many potential advantages. However, the necessity to utilize materials having polar structures limits the choice of piezocatalysts. Herein, we demonstrate that centrosymmetric BiOBr with oxygen defects can simultaneously produce H_2 and H_2O_2 with ultrahigh efficiencies from pure and seawater without needing assistance from noble metals or scavengers. High-pressure studies confirmed that there are no non-polar-to-polar phase transitions in BiOBr, though we discovered a novel isostructural phase. Computational studies revealed that oxygen vacancy distorts the BiOBr structure to induce charge-localization and polarization. Furthermore, high pressure (i) reduces carrier effective masses and (ii) increases relative O-2*p* contribution in the valence band maximum to assist catalysis and improve stability. The role of oxygen vacancy

was confirmed by changing its concentration, which proportionally affected H_2 evolution. Our work paves the way for defect engineering to develop piezocatalysts from a large pool of non-polar materials.

Keywords: piezocatalysis, isostructural phase transition, seawater splitting

Introduction

Catalytic water splitting technology offers a promising solution to the global energy crisis by converting renewable energy into hydrogen (H_2) with high energy capacity and producing benign oxygen (O_2) as a byproduct.[1–4] However, commercial implementation is hindered by challenges such as the need to separate H_2 and O_2 gases, the slow kinetics of the four-electron oxygen evolution reaction, and the unsustainability of using ultrapure water. The two-electron pathway, which produces both H_2 and hydrogen peroxide (H_2O_2), presents a better alternative as it addresses these challenges and yields H_2O_2, a valuable clean liquid fuel and versatile industrial chemical.[5–7] Current H_2O_2 production relies on the anthraquinone oxidation process, which is energy-intensive and poses safety risks due to high-pressure hydrogen handling, making it environmentally detrimental. Additionally, as seawater accounts for 97% of Earth's water resources, there is considerable interest in seawater splitting, especially since oceans also offer a broad spectrum of frequencies suitable for piezocatalysis. In this context, the piezocatalytic seawater splitting using mechanical energy in the form of ultrasonic noise is highly desirable.[8–10]

Piezocatalysis is an emerging approach for fuel production utilizing waste mechanical energy to induce atomic displacement and polarization within a catalyst material, which in turn facilitates effective charge separation.[11-15] Unlike traditional photocatalysis, piezocatalysis doesn't rely on precise band-edge positions because the piezoelectric effect can naturally bend the conduction and valence bands.[16,17] Furthermore, it can work effectively in materials with lower electrical conductivity, expanding the pool of suitable materials, and doesn't require an external energy source, as in electrocatalysis.[18] Several piezocatalysts have been developed recently with H_2 production efficiencies per gram of the catalyst surpassing those in the photocatalytic approach, despite not using any expensive noble metal cocatalysts and hole scavengers. In a few cases, minuscule amounts of H_2O_2 production have also been observed. The H_2O_2 production can, in certain cases, negatively impact the overall efficiency because the same upon decomposition generates molecular O_2 which scavenges the negative charges on the catalyst to form H_2O_2 again, and the cycle reduces both the H_2 and H_2O_2 production.[1,19,20]

Therefore, realizing new catalysts with improved efficiencies for the simultaneous production of these two fuels even from seawater is critical for realizing waste mechanical energy harvesting for fuel generation.

However, a major challenge in designing piezoelectric catalyst materials is that they must possess a crystal structure devoid of a center of symmetry, or else, the pressure-induced polarization in the unit half-cells cancels each other to severely limit the choice of a catalyst.[21,22] Thus, it is essential to explore and develop materials that do not rely on an overall non-centrosymmetric structure alone to develop piezoelectric charges. Herein, we demonstrate that centrosymmetric defect-rich BiOBr can act as a highly efficient bifunctional catalyst for two-electron overall water splitting with simultaneous evolution of H_2 and H_2O_2 under ultrasonic treatment without any co-catalyst and scavenger. The H_2 evolution rate of 2.7 mmol $h^{-1}g^{-1}$ in pure water and 1.7 mmol $h^{-1}g^{-1}$ in seawater is significantly higher than most of the recently developed piezocatalysts and photocatalysts that use noble metals as cocatalysts and scavengers for hole annihilation. The simultaneous H_2O_2 generation rate of 462 μmol $h^{-1}g^{-1}$, and 234 μmol $h^{-1}g^{-1}$, respectively, is also the highest known to date when considering all metal-based catalysts and the fact that only the hydroxyl ion oxidation route is responsible for its generation.

Even though a BiOBr crystal is not expected to exhibit piezocatalytic behavior due to being centrosymmetric, our measurements established that their microparticles prepared under hydrothermal process are highly piezoelectric. We, therefore, explored the possibility of changes in its crystal structure under pressure up to 42.5 GPa, matching those in the piezocatalytic conditions, which revealed an interesting and previously unknown phase transition but remained centrosymmetric throughout. We subsequently explored the possibility of local symmetry breaking in the crystal due to the presence of oxygen vacancies leading to polarization. Notably, such vacancies have been very recently shown to lead to giant piezoelectricity in other oxide phases.[23–25] Chemical analysis of our sample confirmed oxygen sub-stoichiometry and the presence of such vacancies. The extensive computational calculations revealed the origin of local centrosymmetry breakage upon introducing oxygen vacancy, resulting in electronic dipole moments along the x/y and z-axis. Interestingly, these atomistic simulations further revealed that the effective mass of the conductors reduces significantly under high pressure to help charge propagation during catalysis. As a confirmation of this model, we systematically varied the concentration of oxygen vacancies in the sample and demonstrated an improved fuel generation efficiency with increased defect concentration.

Finally, we highlight that since no excitons are involved, BiOBr remains highly stable under catalytic conditions. This is critically important because although BiOX (X = Br, Cl) has been thoroughly explored for high photocatalytic efficiency, it remains unusable due to exciton-induced photo-corrosion, resulting in Cl_2/Br_2 evolution.

Results and discussion

BiOBr belongs to the Sillen phases with a general formula of $[Bi_2O_2]^{2+}[X_2]^{2-}$, consisting of stacked sheets of [Br–Bi–O–Bi–Br] (**Figure 1a)** within the non-polar *P4/nmm* space group, where the mono $[Bi_2O_2]$ layers alternate with double layers of Br along the positive *c*-axis.[26] A Bi atom is coordinated by four oxygen and four bromine ions on either side, forming a $Bi[O_4Br_4]$ decahedron with a net polarization vector pointing towards oxygen. The polarization is however neutralized by neighboring polyhedra along the negative *c*-axis due to its center of symmetry. The [Br–Bi–O–Bi–Br] sheets are held together by van der Waals forces between the Bi & Br atoms from the adjacent sheets leading to high compressibility under pressure. Thus, two distinct Bi-to-Br distances are expected to behave differently under pressure, one within a Bi−O−Br (intra)layer and represented by Bi−Br(I), whereas the same in the two neighboring Bi−O−Br (inter)layers along the [001] direction is represented by Bi−Br(II)**.**

The purity of the BiOBr particles obtained by the hydrothermal synthesis was confirmed by powder X-ray diffraction (XRD, **Figure 1b**, ICDS#98-001-1207).[27] Scanning Electron Microscopy (SEM) and Transmission Electron Microscopy (TEM) analysis revealed that our BiOBr consists of nanoplates with a thickness of ~40 nm (Figure 1c inset) that are radially aligned and tightly packed, forming a hierarchical microsphere with a diameter of ~2-3 μm **(Figure 1c** and **inset, Figure 1d)**. The lattice fringes in a nanoplate with 0.28 nm spacing (high-resolution TEM (HRTEM) image, **Figure 1e**) correspond to the (110) planes of BiOBr. The packing of the nanoplates leads to a mesoporous structure (type-IV N_2 adsorption-desorption isotherm, **Figure 1f)** having an average pore size of 20 nm and a surface area of 6.9 ± 0.3 m^2/g. The oxidation states of the surface atoms were confirmed by X-ray photoelectron spectroscopy (XPS, **Figure S1 a and b,** Supporting Information). In the O-1*s* XPS spectrum **(Figure 1g)**, three distinct peaks at 529.2, 530.6, and 531.9 eV can be discerned, where 529.2 and 531.6 peaks represent the lattice oxygen (O_L) and adsorbed O_2 molecules (O_{add}), respectively.[28,29] The peak at 530.6 eV has been attributed to oxygen atoms adjacent to an oxygen vacancy (O_v) having a higher binding energy to Bi than O_L due to adjacent vacancy.

The valence band maximum (VBM) and the conduction band minimum (CBM) positions were estimated at 2.17 and 0.47 eV *vs.* NHE respectively by relating an average bandgap (E_g) of the microspheres (2.64 eV) to a flat band potential of -0.47 V (**Figure S2,** Supporting Information**).**[30]

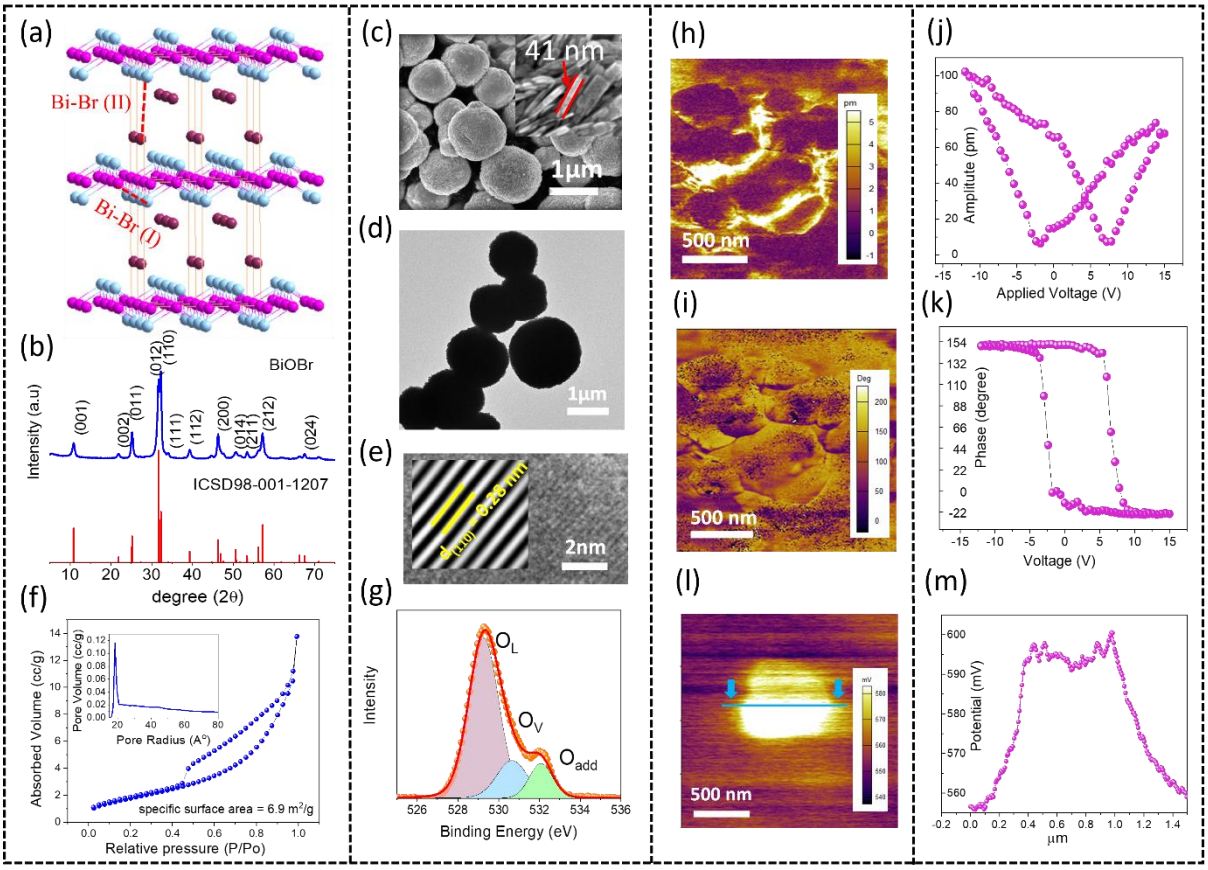

Figure 1: (a) Crystal structure from the *[001]* view direction (dark purple, purple, and blue spheres represent Br, O, and Bi atoms respectively). (b) Powder XRD pattern, (c) SEM, (d) TEM, and (e) HRTEM images of the BiOBr microspheres. (f) N_2 adsorption isotherm with pore-size analysis in the inset. (g) High-resolution XPS spectrum of O-1*s* of the BiOBr sample. (h, i) PFM amplitude, and phase images, respectively, of a BiOBr microsphere. (j, k) Displacement–voltage and phase curves of the microsphere. (l, m) KPFM potential mapping image of a microsphere in the dark and the corresponding surface potential plot.

The unusual piezoelectric properties of the centrosymmetric BiOBr microspheres were confirmed using piezoelectric force microscopy (PFM, **Figure S3 a, b,** & **c,** Supporting Information) and Kelvin probe force microscopy (KPFM, **Figure S3 d & e,** Supporting Information). Therein, pronounced local piezoresponse hysteresis loops were obtained by sweeping the DC bias from -15 V to +15 V while simultaneously recording the phase and amplitude responses (**Figure 1h, i**). A maximum effective piezoelectric coefficient of 63.29

pm/V (with a deviation of ~10%) was determined from the distinctive butterfly-shaped amplitude loop, underscoring the piezoelectric nature of the BiOBr microspheres (**Figure 1j**). Notably, the phase-angle-voltage hysteresis plot exhibited a 180° shift upon reversing the DC bias due to polarization switching within the subject (**Figure 1 k**). To understand the nature of the surface charge, a piezoelectric potential map was acquired by scanning the KPFM cantilever over the nanoplate. The contact potential difference (CPD) between the tip and the nanoplate unveiled a surface potential of 42 mV (**Figure 1 l, m**).

Piezocatalytic Hydrogen Generation: To assess the piezocatalytic efficiency of the BiOBr microspheres, the splitting of pure water and seawater was performed under ultrasonic vibrations without any scavenger or co-catalyst. Notably, a negligible amount of H_2 was also detected (reaching ~33.6 micromoles/g in two hours, **Figure 2 a**) under identical conditions but in the absence of the catalyst. On the other hand, a pronounced H_2 evolution rate of ~6 millimole/g in two hours from pure water establishes that BiOBr plays an important role in ultrasonic water splitting from the reduction of protons by its surface potential developed under ultrasonic pressure. The effect of catalyst loading on H_2 generation was examined (5 to 15 mg range, **Figure 2 b)** to find that increasing catalyst dosage reduces H_2 generation per gram of the catalyst, attributed to the reduction of the effective acoustic power experienced by catalyst particles.[21] Piezocatalytic seawater splitting was also performed by using NaCl solution (3 weight/volume%) as well as real seawater (Arabian Sea) to investigate the effect of salts and other impurities on H_2 production. As seen in **Figure 2 c**, the hydrogen production rate drops from ~3 mmol/h/g in pure water to ~2 mmol $h^{-1}g^{-1}$ in NaCl solution and 1.5 mmol $h^{-1}g^{-1}$ in real seawater. We attribute the reduced production rate in seawater to the blockage of active sites and screening of piezo-changes by the ions, as demonstrated in our previous study.[11] We further conducted trapping experiments to determine the active species responsible for pure water splitting by using lactic acid as positive and $AgNO_3$ as negative charge-trapping reagents respectively (**Figure 2 d)**. It revealed that positive charge scavenging further increases H_2 generation, due to suppression of the recombination of induced charges.[1,11] Conversely, the presence of $AgNO_3$ noticeably inhibited the H_2 generation rate, confirming that the induced negative charges are the primary active species for H_2 evolution.

We also explored the impact of ultrasonication frequency and power on catalytic efficiency. H_2 production is high when a frequency of 37 kHz is used as compared to 80 kHz (**Figure 2 e)**, attributed to proximity to the resonance frequency of the catalyst.[11] Additionally, the production rate at 37 kHz increases as power is increased from 40% (44 W) to 100% (110

W, **Figure 2 f**), where the increase is rather nonlinear with an initial rate of 392 μmol $h^{-1}g^{-1}$ improving enormously to 2.7 mmol $h^{-1}g^{-1}$ at the end. Also, a rate of 2.7 mmol h^{-1} g^{-1} and 1.7 mmol h^{-1} g^{-1} in pure water and seawater respectively is one of the best performances reported to date (**Figure 2 g, Table S 1,** Supporting Information). Considering piezoelectric charges, $Q_p = dT$ (where d is the piezoelectric coefficient and T is external stress), higher vibrational power can lead to higher T, which induces more piezoelectric charges, resulting in a higher hydrogen production rate. However, the processes of transient stress accumulation and transfer within a particle, and also, defects or surface structural changes during piezocatalysis that are potentially responsible for the nonlinear increase are not well understood yet. In addition, we recently hypothesized that the fraction of the catalyst particles that are suitably exposed to ultrasonic pressure to experience sufficient band-bending for proton reduction may vary nonlinearly due to multiple bubbles bursting at higher power, leading to a non-linear effect.[11]

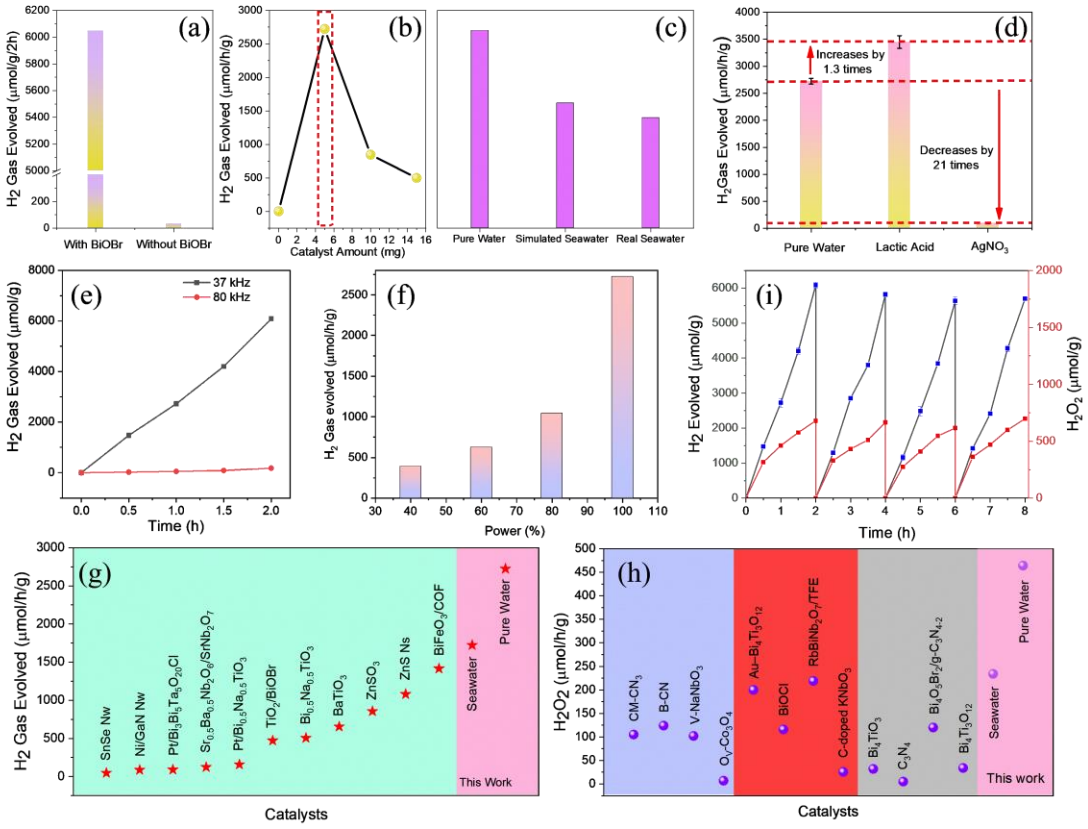

Figure 2: (a) Ultrasound-induced H_2 production rate in the presence or absence of piezocatalysts. (b) H_2 production rate in pure and seawater. (c) Effect of catalyst dosage on H_2 production. (d) Plot showing the effect of charge trapping agents on H_2 production. (e, f) Hydrogen production in different ultrasonic frequencies and power respectively. Comparison of the (g) H_2 production and (g) H_2O_2 production performances of BiOBr with other state-of-the-art catalysts. (h) Simultaneous H_2 and H_2O_2 production by BiOBr for 8 h.

Importantly, as a counter-reaction, the oxidation of water resulted in the concurrent generation of H_2O_2, indicating that the positive charges induced by the piezopotential oxidized hydroxide ions (OH^-) to produce H_2O_2. The H_2O_2 production rates were estimated to be a high 462 μmol $h^{-1}g^{-1}$ and 234 μmol $h^{-1}g^{-1}$ in pure water and seawater respectively **(Figure S4,** Supporting Information**),** which is comparable in performance considering even those catalysts that are developed for H_2O_2 production alone (**Figure 2h, Table S2,** Supporting Information). It may be noted that H_2O_2 production may occur from the reduction of molecular O_2, which in usual cases contributes majorly to the yield but competes with proton reduction to decrease the H_2 yield, or can also be generated by the oxidation of OH^- ions. In the present study, since no additional O_2 flow was used, the H_2O_2 production entirely occurs from OH^- oxidation. Thus, the ultrasonic process leads to the generation of two useful chemicals with considerably reduced separation difficulties. However, since the H_2O_2 production rate is somewhat lower than the H_2 production rate, we estimated the dissolved O_2 (DO) level in the reaction mixture, which might have been generated from H_2O_2 decomposition.[31] As seen in **Figure S5**, (Supporting Information) a gradual increase in the DO level confirms that a fraction of the produced H_2O_2 gets decomposed. The recyclability of the catalyst was established from four consecutive cycles as seen in **Figure 2i**.

Notably, no significant structural changes were found in the catalyst after recycling (**Figure S6, S7,** Supporting Information), which deserves to be highlighted because BiOCl/Br has been widely used as a photocatalyst for renewable energy harvesting. However, its stability against photo-corrosion remains a bottleneck,[32–34] and therefore the high stability of these materials under piezocatalytic conditions is a critical finding for its sustainable use. The photo-corrosion has been shown to originate from populating the halide sub-bands in the valence bands by the excitonic hole that results in chlorine gas evolution.[35] In that context, our high-pressure studies discussed *vide infra* have demonstrated that under ultrasonic pressure the contribution of oxygen to the valence band maximum significantly increases, which induces high stability of the lattice chloride against photo-corrosion. A similar effect was demonstrated recently both experimentally and theoretically in the related Sillen Aurivillus phases where the introduction of the Aurivillus phase increases the oxygen contribution in the valence band than that from chlorine to render improved stability. [35–37]

Structural Changes at High Pressure and Origin of Efficient Piezocatalysis: To probe the potential structural changes occurring in centrosymmetric BiOBr under piezocatalytic conditions and to understand the origin of piezocatalysis, *in-situ* high-pressure powder X-ray

diffraction measurements were performed. Even though such a correlation has not been established in piezocatalytic systems, conventional high-pressure studies on many piezoelectric systems indicate phase transitions under high pressure.[38] Our synchrotron measurements were conducted at pressure values ranging from 0.2 to 42.5 GPa (within errors ~0.1 GPa), closely matching those under piezocatalytic conditions.[11,39] **Figure 3a** displays the evolution of the X-ray diffraction patterns throughout this pressure range, establishing interesting but unusual peak shifts for different crystal planes.[40] No appearances of extra ones or disappearances of the existing Bragg peaks were observed, apart from some sharp peaks that emerged from 7.4 GPa onwards, corresponding to the crystallization of Ne, used as a pressure-transmitting medium.[41] Interestingly, by using Rietveld refinement, the diffraction patterns could be modeled with the same non-polar *P4/nmm* space group at all pressures, suggesting minimal changes in the relative orientation of the constituting atoms throughout (**Figure S8** and **Table S3,** Supporting Information).

Nevertheless, the variations in the "*a"* and the "*c"* parameters exhibited a noticeable discontinuity beyond ~16.2 GPa (**Figure 3b**). A nearly linear decrease in the "*a*" values undergoes a sudden change in slope from a higher decay rate to a lower one. On the other hand, the decrease in "*c*" is significantly rapid and non-linear until 16.2 GPa, beyond which the shrinkage rate slows down. The "*c/a*" ratio exhibited a nonlinear decrease during the initial compression, indicating that "*c*" is more compressible than "*a*" (**Figure 3c)** due to the weaker interlayer van der Waals forces relative to the stronger intralayer covalent bonding. Above 16.2 GPa, the "*c/a"* change rate followed a near-linear decrease, suggesting that the cell parameters "*a*" and "*c*" undergo nearly isotropic contractions in the high-pressure region. Additionally, the Bi−Br(I) bond distance decrease follows apparent linearity before and after 16.2 GPa but with different rates. In contrast, Bi−Br(II) distances decrease non-linearly and linearly before and after 16.2 GPa respectively, having larger compression than Bi−Br(I). The changes are schematically presented in **Figure S8b**. Similarly, Bi−O distance decreases with increasing pressure with apparent change in slope at 16.2 GPa (**Figure 3d)**.

Previously, similar structural changes were observed in the case of BiOCl, attributed to an isostructural phase transition,[38] and accordingly, a low-pressure phase (LPP) and a high-pressure phase (HPP) are defined here for BiOBr too across ~16.2 GPa. The pressure *vs.* unit cell volume (P−V) data fits well to a third-order Birch−Murnaghan equation of state (BM-EoS, **Figure 3e**) to reveal the zero-pressure volume (V_0), bulk modulus (B_0), and its pressure derivative (B_0'). B_0 was estimated as 23(4) and 58(1) GPa for the LPP and HPP respectively,

while that for B_0' are 15(3) and 7.1(2), respectively. The V_0 of these two phases 125.4(8) and 119.7(1) Å^3) are higher by 14.4 and 8.7 values than BiOCl in the lower-pressure region and higher-pressure region respectively.

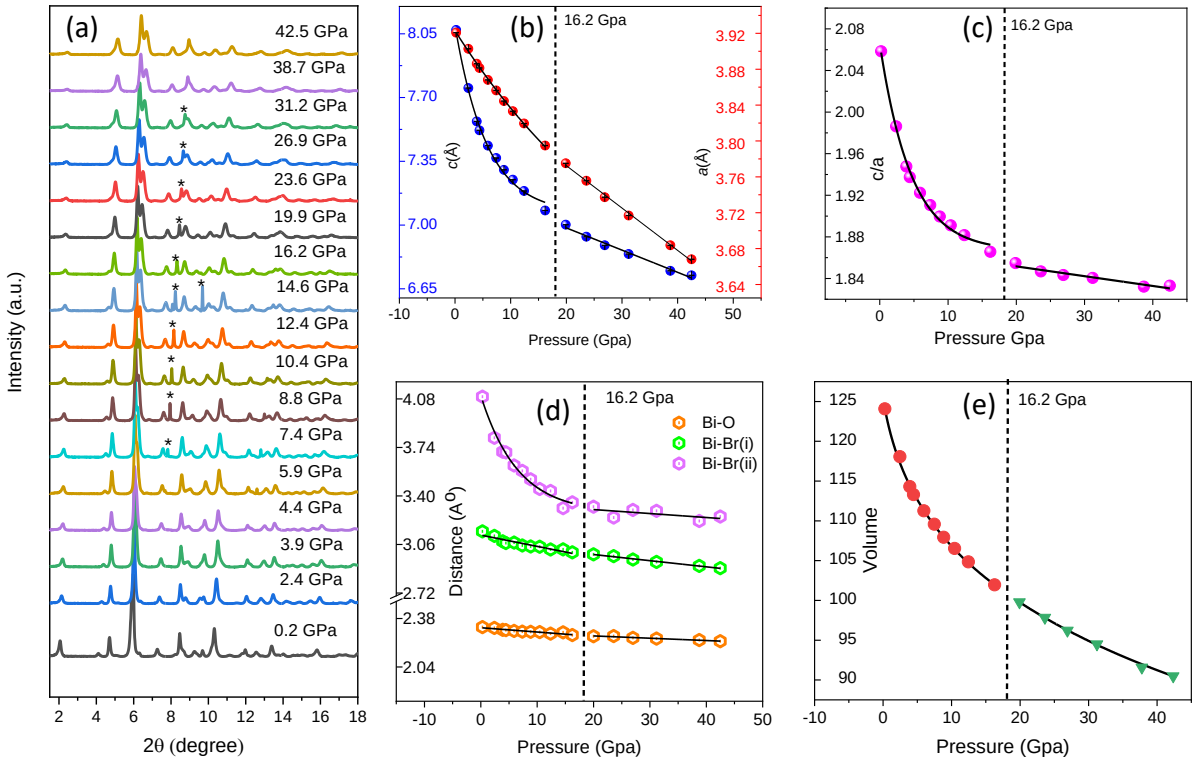

Figure 3: (a) *In-situ* high-pressure X-ray powder diffraction of BiOBr at room temperature up to 42.5 GPa. Pressure dependences of (b) lattice parameters, (c) the *c* to *a* ratio, and (d) bond distance of BiOBr up to 42.5 GPa (the solid lines are guides to the eye). (e) The corresponding pressure dependence of unit cell volume (V), fitted according to the BM-EoS equation of state (error bars are within the symbols in all plots).

On observing isostructural phases under high pressure, we carried out detailed computational simulations that revealed important insights into the atomistic structure-property relationships. The unconstraint geometry optimization under different pressures closely follows the change in experimental lattice parameters. Overall, we find relatively excess *c*-axis compressibility with higher external pressures (**Figure S9,** Supporting Information). The non-covalently stacked layers of BiOBr along the *c*-axis result in this anisotropic lattice compression. Exploring the tuning in electronic properties, we calculated the Bader charges on different elements. These analyses (**Figure 4a**) exhibit that the constituting atoms experience a greater degree of charge separation under applied external pressure, leading to an increased positive charge on Bi, and a higher negative charge on O. Br atoms also exhibit increased negative charge, but to a lesser extent compared to more electronegative oxygen atoms. The

charge redistribution under pressure results in a robust internal potential and a high built-in electric field within a BiOBr layer.

Interestingly, the valence bands (VB) and the conduction bands (CB) around the Fermi energy (E_F) displayed several pronounced pressure-dependent electronic effects (**Figure 4b and Figure S10,** Supporting Information).[42] In this indirect band-gap material, the CB minimum (CBM) is nearly maintained at the Z point in the Brillouin zone,[43] while its VB maximum (VBM) shifts slightly towards the Z point along the R−Z path, indicating a probable indirect to direct bandgap transition at much higher pressure **(inset Figure 4b)**. **Figure 4c** and **Figure S11** (Supporting Information) present the accompanying significant changes in the density of states (DOS), where the predominant contribution to the VBM from Br-*p* orbitals at ambient conditions decreases rapidly under pressure, while the contributions of Bi-*s* and O-*p* orbitals gradually increase. Since the electronegativity of oxygen is higher than that of bromine and the contribution of oxygen to the VBM increases with pressure, the valence band edge gets stabilized energetically. Similarly, in the CBM, increasing pressure leads to a decrease in the Bi-*p* orbital contribution and a concomitant increase in the contributions from Br-p orbitals. Overall, increasing pressure stabilizes the VBM more than the CBM and the E*g* of the LPP of BiOBr increases with increasing pressure. Note that, the increase in the bandgap gets saturated at the high-pressure phase as the VBM and CBM stabilize by a similar extent at that pressure range (**Figure S12,** Supporting Information**)**. The increase in O-2p contribution to the VBM at high pressure is attributed to the high stability of BiOBr under ultrasonic conditions because oxygen involves a sluggish two-electron transfer to leach, while bromine needs just one.

The band structure analysis underscores another important aspect of piezocatalysis. In **Figure 4d**, a notable trend in the effective mass of electrons along the stacking direction and the xy plane is observed within the CBM and VBM, respectively. As the pressure increases, there is a consistent decrease in effective mass, more pronounced in the CB, potentially leading to efficient electron transport within the material. The same would be beneficial in conditions that combine photoexcitation and mechanical stress, such as piezo-photocatalysis in contrast to conventional photocatalysis, representing a potential enhancement in efficiency.

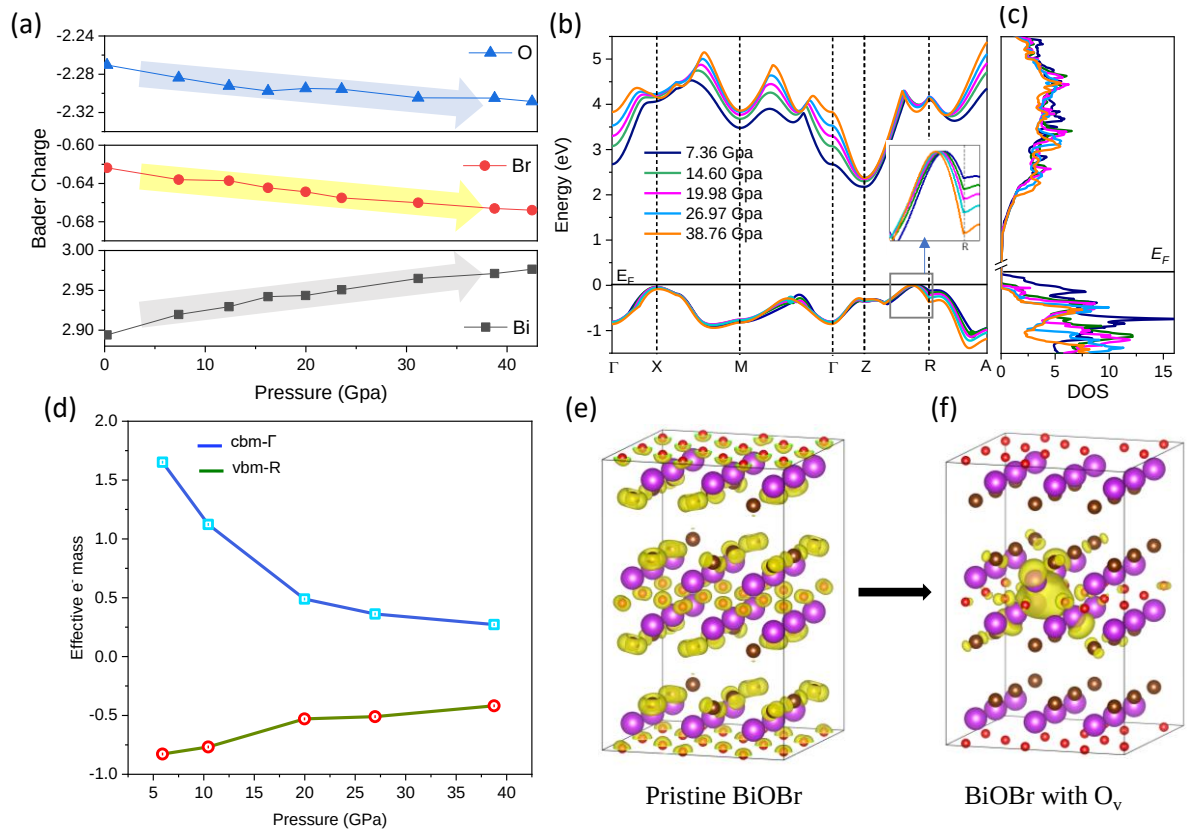

Figure 4: (a) Pressure dependences of Bader charge for Bi, O, and Br ions of BiOBr. (b) Highest valence bands and lowest conduction bands, and (c) calculated density of states around the Fermi energy (E_F) of BiOBr at different pressures. (d) Plot showing decreases in the effective mass of carriers in VBM and CBM with increasing pressure (inset highlights the corresponding band-structure region showing changes in curvature and shift in VBM position). Delocalized band-decomposed charge density near the band edges for (e) pristine BiOBr supercell and (f) BiOBr supercell with an oxygen vacancy showing highly localized charge density at the O_v site.

Generally, a centrosymmetric space group is not expected to exhibit piezoelectricity.[16] Besides, the aforementioned diffraction and computational studies confirm that there is no evidence of symmetry breakage in BiOBr under high pressure. However, the PFM and piezocatalytic investigations demonstrated that BiOBr does respond to external pressure by concurrently producing H_2 and H_2O_2. In this context, several emerging studies propose that O_v in centrosymmetric oxide crystals can induce piezoelectric responses. For instance, an exceptionally large piezoelectric response was obtained in centrosymmetric CeO_{2-x} films by introducing O_v, resulting from an expansion of surrounding chemical bonds. This response is two orders of magnitude larger than that in the best-known piezoelectric relaxor–ferroelectric

oxides at kilohertz frequencies.[23] Metal atoms around an O_v are displaced away due to Coulomb repulsions so that the M-O_v-M distance is larger than the M-O-M distance.[44] This distortion produces an anisotropic elastic dipole with tensile strain along the pristine M-O_v-M direction. Notably, the piezocatalytic degradation capability of organic dyes using BiOBr was also observed.[45] However, the origin of polarization in centrosymmetric BiOBr is yet to be explored.

We have now carried out a computational analysis by introducing an O_v on the supercell of BiOBr, since this is the most common defect in this material and in our samples too.[24] The computationally optimized structure of the oxygen-deficient system revealed the off-centering of the Bi atom in the oxygen polyhedral towards the larger number of oxygen atoms within the *xy* plane, resulting in the total electronic dipole moment of -6.03 eÅ and -18.09 eÅ along the x/y and z-axis, respectively (**Figure 4e** and **f**). The computed net electronic dipole moment under external pressures exhibits similar finite values for BiOBr lattice with O_v defect (**Table S4**, Supporting Information). Moreover, the electronic pDOS plot for BiOBr depicts that the O_v introduces midgap defect states (**Figure S13 a**, Supporting Information) and localizes electron densities near the vacant site (**Figure 4f**). These occupied midgap states are mostly contributed by the Bi-6(*s,p*) orbitals that form dangling bonds due to the presence of O_v. To quantify the extent of electronic localization, we calculated the inverse participation ratio (IPR) for electronic states near the Fermi level of BiOBr. The higher the IPR, the stronger the electronic localization of a Kohn-Sham state. As shown in **Figure S13 b** (Supporting Information), the extent of electronic localization at the defect state remains mostly unchanged with imposed external pressures, emphasizing the robustness of these electronic characters under structural perturbations. Thus, this defect-induced symmetry-breaking and associated net dipole moment creation are potentially responsible for piezocatalysis on BiOBr samples. If this is the case, one should be able to control the piezocatalytic efficiency of BiOBr by controlling O_v density.

To verify this, we conducted a series of experiments involving the generation of three samples with varying O_v by subjecting the fresh-BiOBr sample to oxidation using hydrogen peroxide of different concentrations at room temperature.[46] We anticipated that H_2O_2 treatment would oxidize the sample and reduce O_v concentration, leading to a decrease in H_2 evolution efficiency. These samples were characterized by TEM, BET, XPS, and XRD (**Figure S14,** Supporting Information) to confirm structural integrity. High-resolution XPS data of the O-1*s* peak for the three samples (**Figure 5a** and **S15,** Supporting Information**)** indicates a

reduction in the concentration of oxygen atoms adjacent to O_v in comparison to both lattice and surface-adsorbed oxygen as oxidation increases, implying a decrease in O_v abundance than in fresh BiOBr.[47] Electron paramagnetic resonance (EPR, **Figure 5b**) spectroscopy confirms the same, revealing in the form of a distinct peak at a g-factor of 2.002 associated with O_v that decreases in intensity with increasing the concentration of H_2O_2 used for treating the fresh BiOBr sample.[48,49]

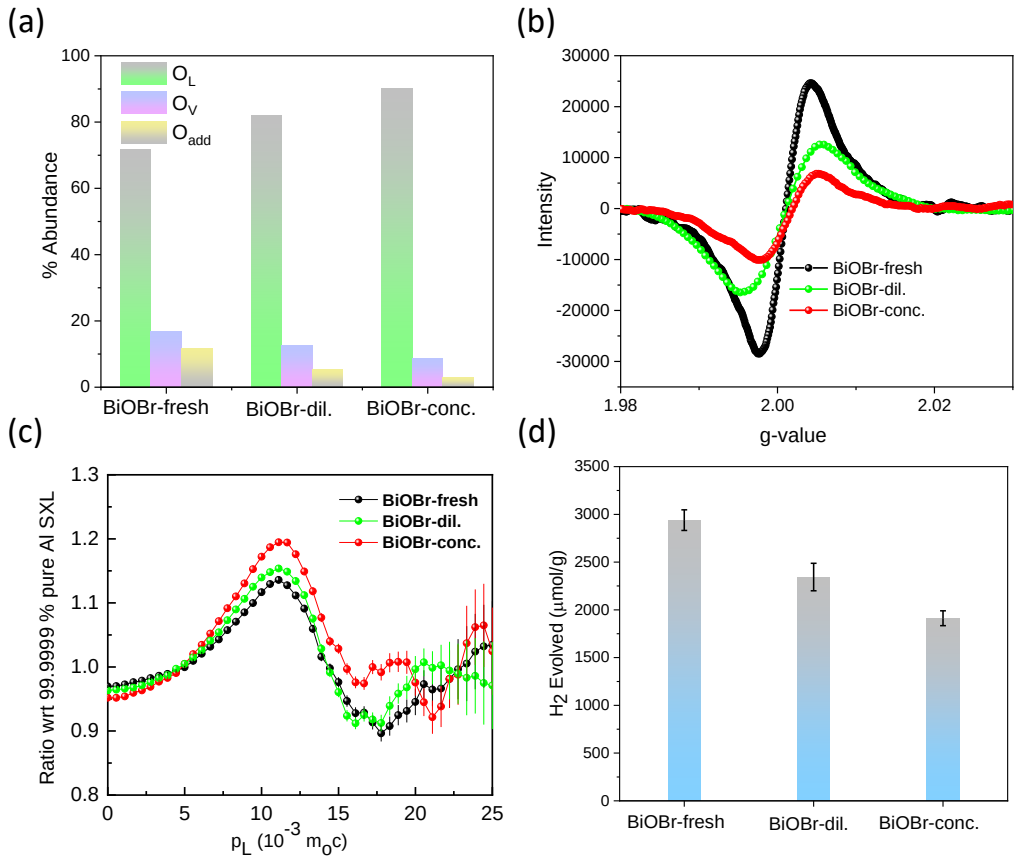

Figure 5: (a) Plot illustrating the diminishing abundance of oxygen vacancies with respect to lattice oxygen and adsorbed molecular oxygen. The electron paramagnetic resonance spectra (b) and coincidence doppler broadening spectra (c) further confirm the decrease in oxygen vacancy levels with the oxidative treatment of the BiOBr microspheres. (d) Plot showing a reduction in H_2 production due to decreasing concentrations of oxygen vacancy.

Positron annihilation spectroscopy was used to characterize the chemical nature of the defects. The analysis of positron annihilation lifetime spectra (PAL) unveiled three distinctive lifetime components in all three BiOBr samples (**Table 1**), providing crucial insights into the defect structure. The most intense τ_2 component is identified as arising from O_v, while the shortest τ_1 corresponds to the free annihilation of positrons in a defect-free state. The longest

component (τ_3) lasting for ~1900 ps and exhibiting minor intensity (~2%) is attributed to the positronium atom pick-off annihilation. The relative decrease in the τ_2 intensity coupled with a concurrent increase in that of τ_1 signifies a progressive reduction in oxygen vacancies induced by H_2O_2 treatment.[50–52] Coincidence Doppler broadening (CDB, **Figure 5c**) spectra were analyzed by calculating point-by-point intensity ratios using an Al single crystal as a reference. The resulting ratio curve of CDB for each of the three samples revealed a distinctive peak at $p_L = 11\times10^{-3}\ m_0c$, attributable to positron annihilation with oxygen anions' 2*p* electrons. The increase in peak intensity observed sequentially from the fresh sample to the H_2O_2-treated samples confirms a decrease in vacancy concentration with an increase in H_2O_2 treatment.

The piezocatalytic hydrogen evolution efficiencies by these catalysts were further evaluated to correlate with their O_v concentration. As seen from **Figure 5d**, it is evident that the hydrogen evolution decreases with decreasing oxygen vacancy concentration, confirming the role of oxygen vacancies as the origin of piezocatalysis in centrosymmetric BiOBr microspheres. The mechanism for Ov-induced piezoelectricity generation and band-bending for H_2 production is schematically illustrated in Supporting Note 1 and Figure S16. Briefly, during piezocatalysis, cavitation bubbles generate mechanical stress on BiOBr, leading to the development of piezopotential on the catalyst's surface. This, in turn, causes bending of the valance and conduction bands of BiOBr contributed primarily by Br and Bi respectively.[11] The valance band bending requirement in BiOBr for efficient water splitting is ~2.6 V so that Br can act as an active site, while up to ~12 V may be achievable using a minimal 1 GPa pressure, making BiOBr an promising catalyst.

Sample	τ_1(ps)	I_1 (%)	τ_2(ps)	I_2 (%)	τ_3(ps)	I_3 (%)
BiOBr- fresh	100 ± 2	15 ± 1	308 ± 1	84 ± 1	1888 ± 48	1 ± 0.06
BiOBr-dil.	100 ± 5	17 ± 1	308 ± 1	82 ± 1	1896 ± 42	1 ± 0.1
BiOBr-conc.	105 ± 5	22 ± 1	330 ± 2	76 ± 1	1979 ± 60	2 ± 0.06

Table 1: Positron annihilation lifetime parameters of the BiOBr-fresh, and the sample treated with dilute (BiOBr-dil.) and concentrated (BiOBr-conc.) H_2O_2.

Finally, we extended the study to centrosymmetric BiOCl because its high-pressure structure has already been elucidated, which is similar to BiOBr.[38] The details of their synthesis and characterization are included in Supporting Note 2 and Figure S17 a,b,c. We found that the H_2 production rate of ~2 mmol $h^{-1}g^{-1}$ by the as-synthesized BiOCl having a

higher Ov abundance. When we intentionally reduced the Ov abundance significantly by H_2O_2 treatment, the production rate decreased to 1.3 mmol $h^{-1}g^{-1}$ (Figure S17), asserting that oxygen-vacancy-induced symmetry breaking can be extended to other centrosymmetric systems to produce H_2 by the piezocatalytic approach efficiently.

Conclusions

In conclusion, we demonstrate that high piezocatalytic properties can be induced in centrosymmetric BiOBr by introducing oxygen vacancies and the same can be used for simultaneous production of H_2 (2.7 mmol $h^{-1}g^{-1}$ (in pure water) 1.7 mmol $h^{-1}g^{-1}$ (in seawater)) and H_2O_2 (462 μmol $h^{-1}g^{-1}$ (in pure water) and 234 μmol $h^{-1}g^{-1}$ (in seawater)) with high efficiencies, despite not using any noble metal cocatalyst and hole scavengers. An oxygen vacancy locally distorts the electron cloud surrounding it to produce polarization. In addition, applying high pressure can improve charge separation by reducing the effective mass of the carriers to further improve catalytic efficiency. Importantly for the BiOBr family of compounds, high pressure leads to excess oxygen 2*p* contribution to the valence band upon unit cell contraction. This is beneficial for catalytic stability, unlike in the case of photocatalysis where the valence band is Cl-3*p* dominated, leading to photocorrosion from oxidative chlorine evolution. A novel isostructural BiOBr phase was discovered while attempting to identify potential changes in its crystal structure to a non-symmetric one at high pressures as the origin of its piezocatalytic activity. These observations should inspire the development of many new piezocatalysts by oxygen vacancy engineering that are otherwise piezo-inactive.

Author contributions

U.K.G. supervised the research. U.K.G. and M.Banoo designed the experiments. M.Banoo, A.K.S, R.S.R contributed to performing the catalytic experiments and XPS characterization. D.G.B performed Rietveld refinement. D.S. performed positron annihilation measurements. D.G. and K.S. performed theoretical studies. M. Bhakar and G.S. performed piezoelectric force microscopy measurements. U.K.G., K.G. and D.T. were involved in high-pressure XRD measurements. M. Banoo did material characterization. All authors discussed the results and commented on the manuscript.

Acknowledgments

M.B. thanks CSIR (India) for the senior research fellowship. Support from SERB, India, under the grant C.R.G./2021/001420, is gratefully acknowledged. We would also like to acknowledge the central facilities at IISER Mohali. Portions of this research were carried out at the beamline P02.2 of PETRA III, DESY, a member of the Helmholtz Association (H.G.F.). Financial support by the DST, India, provided within the framework of the India@DESY collaboration, is gratefully acknowledged. DG acknowledges the IIT Delhi SEED Grant (PLN12/04MS), the Science and Engineering Research Board (SERB), Department of Science and Technology (DST), India for Start-up Research Grant SRG/2022/00l234 and the IIT Delhi HPC facility for computational resources.

Conflicts of interest

The authors declare that they have no competing interests.

References

[1] C. Hu, F. Chen, Y. Wang, N. Tian, T. Ma, Y. Zhang, H. Huang, *Adv. Mater.* **2021**, *33*, 1.

[2] L. Wang, Y. Zhang, L. Chen, H. Xu, Y. Xiong, *Adv. Mater.* **2018**, *30*, 1.

[3] T. Oshima, D. Lu, O. Ishitani, K. Maeda, *Angew. Chemie* **2015**, *127*, 2736.

[4] G. Wan, L. Yin, X. Chen, X. Xu, J. Huang, C. Zhen, H. Zhu, B. Huang, W. Hu, Z. Ren, H. Tian, L. Wang, G. Liu, H. M. Cheng, *J. Am. Chem. Soc.* **2022**, *144*, 20342.

[5] C. Hu, J. Hu, Z. Zhu, Y. Lu, S. Chu, T. Ma, Y. Zhang, H. Huang, *Angew. Chemie - Int. Ed.* **2022**, *61*.

[6] J. He, F. Gao, H. Wang, F. Liu, J. Lin, B. Wang, C. Liu, F. Huang, Z. Lin, M. Wang, *Environ. Sci. Nano* **2022**, *9*, 1952.

[7] F. Xue, Y. Si, M. Wang, M. Liu, L. Guo, *Nano Energy* **2019**, *62*, 823.

[8] S. Wu, H. Yu, S. Chen, X. Quan, *ACS Catal.* **2020**, *10*, 14380.

[9] L. Wang, J. Zhang, Y. Zhang, H. Yu, Y. Qu, J. Yu, *Inorganic Metal-Oxide Photocatalyst for H2O2 Production*, Vol. 18, John Wiley and Sons Inc, **2022**.

[10] X. Zhou, F. Yan, A. Lyubartsev, B. Shen, J. Zhai, J. C. Conesa, N. Hedin, *Adv. Sci.* **2022**, *9*, 1.

[11] M. Banoo, R. S. Roy, M. Bhakar, J. Kaur, A. Jaiswal, G. Sheet, U. K. Gautam, *Nano Lett.* **2022**, *22*, 8867.

[12] J. Li, G. Xie, J. Jiang, Y. Liu, C. Chen, W. Li, J. Huang, X. Luo, M. Xu, Q. Zhang, M. Yang, Y. Su, *Nano Energy* **2023**, *108*.

[13] J. Dai, G. Xie, C. Chen, Y. Liu, H. Tai, Y. Jiang, Y. Su, *Appl. Phys. Lett.* **2024**, *124*.

[14] J. Li, H. Yuan, Q. Zhang, K. Luo, Y. Liu, W. Hu, M. Xu, S. Xu, *Phys. Chem. Chem. Phys.* **2020**, *22*, 27272.

[15] M. Banoo, A. K. Sah, R. S. Roy, P. Bhardwaj, D. G. Porob, G. Sheet, U. K. Gautam, *Chem. Mater.* **2024**.

[16] S. Tu, Y. Guo, Y. Zhang, C. Hu, T. Zhang, T. Ma, H. Huang, *Adv. Funct. Mater.* **2020**, *30*, 1.

[17] K. Wang, C. Han, J. Li, J. Qiu, J. Sunarso, S. Liu, *Angew. Chemie - Int. Ed.* **2022**, *61*.

[18] M. B. Starr, X. Wang, *Sci. Rep.* **2013**, *3*.

[19] C. Wang, C. Hu, F. Chen, H. Li, Y. Zhang, T. Ma, H. Huang, *Adv. Funct. Mater.* **2023**, *2*, 1.

[20] W. Feng, J. Yuan, L. Zhang, W. Hu, Z. Wu, X. Wang, X. Huang, P. Liu, S. Zhang, *Appl. Catal. B Environ.* **2020**, *277*, 119250.

[21] Y. Zhang, H. Khanbareh, S. Dunn, C. R. Bowen, H. Gong, N. P. H. Duy, P. T. T. Phuong, *Adv. Sci.* **2022**, *9*, 1.

[22] R. Su, H. A. Hsain, M. Wu, D. Zhang, X. Hu, Z. Wang, X. Wang, F. tang Li, X. Chen, L. Zhu, Y. Yang, Y. Yang, X. Lou, S. J. Pennycook, *Angew. Chemie - Int. Ed.* **2019**, *58*, 15076.

[23] D. S. Park, M. Hadad, L. M. Riemer, R. Ignatans, D. Spirito, V. Esposito, V. Tileli, N. Gauquelin, D. Chezganov, D. Jannis, J. Verbeeck, S. Gorfman, N. Pryds, P. Muralt, D. Damjanovic, *Science (80-.).* **2022**, *375*, 653.

[24] H. Wang, D. Yong, S. Chen, S. Jiang, X. Zhang, W. Shao, Q. Zhang, W. Yan, B. Pan, Y. Xie, *J. Am. Chem. Soc.* **2018**, *140*, 1760.

[25] Z. Shen, Z. Luo, J. Chen, Y. Li, *Adv. Funct. Mater.* **2023**, *33*.

[26] Z. K. Tang, W. J. Yin, Le Zhang, B. Wen, D. Y. Zhang, L. M. Liu, W. M. Lau, *Sci. Rep.* **2016**, *6*, 1.

[27] X. Cao, A. Huang, C. Liang, H. C. Chen, T. Han, R. Lin, Q. Peng, Z. Zhuang, R. Shen, H. M. Chen, Y. Yu, C. Chen, Y. Li, *J. Am. Chem. Soc.* **2022**, *144*, 3386.

[28] M. Banoo, K. Chatterjee, S. Mondal, C. P. Vinod, U. K. Gautam, *Green Chem.* **2022**, *24*, 5514.

[29] X. J. Wang, Y. Zhao, F. T. Li, L. J. Dou, Y. P. Li, J. Zhao, Y. J. Hao, *Sci. Rep.* **2016**, *6*, 1.

[30] Y. Li, H. Jiang, X. Wang, X. Hong, B. Liang, *RSC Adv.* **2021**, *11*, 26855.

[31] Y. Shiraishi, Y. Ueda, A. Soramoto, S. Hinokuma, T. Hirai, *Nat. Commun.* **2020**, *11*, 1.

[32] X. Zhao, Z. Zhao-Karger, D. Wang, M. Fichtner, *Angew. Chemie - Int. Ed.* **2013**, *52*, 13621.

[33] Y. Zhou, H. Wang, X. Liu, D. Zeng, K. Wang, L. Zhang, W. Wang, *Appl. Catal. B Environ.* **2021**, *294*, 120265.

[34] L. Ye, Y. Su, X. Jin, H. Xie, C. Zhang, *Environ. Sci. Nano* **2014**, *1*, 90.

[35] H. Fujito, H. Kunioku, D. Kato, H. Suzuki, M. Higashi, H. Kageyama, R. Abe, *J. Am. Chem. Soc.* **2016**, *138*, 2082.

[36] D. Kato, K. Hongo, R. Maezono, M. Higashi, H. Kunioku, M. Yabuuchi, H. Suzuki, H. Okajima, C. Zhong, K. Nakano, R. Abe, H. Kageyama, *J. Am. Chem. Soc.* **2017**, *139*, 18725.

[37] H. Kunioku, M. Higashi, O. Tomita, M. Yabuuchi, D. Kato, H. Fujito, H. Kageyama, R. Abe, *J. Mater. Chem. A* **2018**, *6*, 3100.

[38] J. Zhao, L. Xu, Y. Liu, Z. Yu, C. Li, Y. Wang, Z. Liu, *J. Phys. Chem. C* **2015**, *119*, 27657.

[39] M. Banoo, J. Kaur, A. K. Sah, R. S. Roy, M. Bhakar, B. Kommula, G. Sheet, U. K. Gautam, *ACS Appl. Mater. Interfaces* **2023**, *15*, 32425.

[40] X. Wang, X. Chen, Y. Zhou, C. Park, C. An, Y. Zhou, R. Zhang, C. Gu, W. Yang, Z.

Yang, *Sci. Rep.* **2017**, *7*, 2.

[41] L. W. Finger, R. M. Hazen, G. Zou, H. K. Mao, P. M. Bell, *Appl. Phys. Lett.* **1981**, *39*, 892.

[42] W. Wang, R. Dai, L. Zhang, Q. Wu, X. Wang, S. Zhang, T. Shao, F. Zhang, J. Yan, W. Zhang, *J. Mater. Sci.* **2020**, *55*, 11226.

[43] B. Hu, Q. Guo, K. Wang, X. Wang, *J. Mater. Sci. Mater. Electron.* **2019**.

[44] M. Tyunina, *Materials (Basel).* **2020**, *13*, 1.

[45] B. Yang, W. Wang, Z. Hu, B. Shen, S. Q. Guo, *J. Hazard. Mater.* **2023**, *458*, 132008.

[46] J. Lee, Y. Choi, B. J. Park, J. W. Han, H. S. Lee, J. H. Park, W. Lee, *J. Adv. Ceram.* **2022**, *11*, 769.

[47] A. Ghobadi, T. G. Ulusoy, R. Garifullin, M. O. Guler, A. K. Okyay, *Sci. Rep.* **2016**, *6*, 1.

[48] Oxygen Vacancy-Mediated Photocatalysis of BiOCl: Reactivity, Selectivity, and Perspectives, .

[49] D. Cui, K. Xu, X. Dong, D. Lv, F. Dong, W. Hao, Y. Du, J. Chen, *Commun. Chem.* **2020**, *3*.

[50] S. Q. Guo, X. H. Zhu, H. J. Zhang, B. C. Gu, W. Chen, L. Liu, P. J. J. Alvarez, *Environ. Sci. Technol.* **2018**, *52*, 6872.

[51] M. Guan, C. Xiao, J. Zhang, S. Fan, R. An, Q. Cheng, J. Xie, M. Zhou, B. Ye, Y. Xie, *J. Am. Chem. Soc.* **2013**, *135*, 10411.

[52] Y. Shi, J. Li, C. Mao, S. Liu, X. Wang, X. Liu, S. Zhao, X. Liu, Y. Huang, L. Zhang, *Nat. Commun.* **2021**, *12*, 1.